Journal of Vibration and Acoustics. Received September 27, 2025;
Accepted manuscript posted March 2, 2026. doi:10.1115/1.4071279

Cross-Domain Simulation of a Plucking Piezoelectric Energy Harvester: Coupling Dynamics, Power Management, and Application

Hao Tang[1,#], Yawei Wang[1,#], Yizhou Li[1], Guobiao Hu[1,*]

[1]*Internet of Things Thrust, The Hong Kong University of Science and Technology (Guangzhou), Guangzhou, Guangdong 511400, China*

[#]*These authors contribute equally to this paper.*

**Correspondence: guobiaohu@hkust-gz.edu.cn (G.H.)*

Abstract: Piezoelectric energy harvesters (PEHs) represent a compelling alternative to batteries for powering low-power IoT electronics, particularly in maintenance-constrained applications. However, the inherently cross-disciplinary scope of the research in this field has impeded the development of a unified multi-physics model that accounts for external excitation, mechanical-to-electrical energy conversion, nonlinear interface circuit behavior, energy management, and system-level power dynamics. This study introduces a system-level simulation framework to overcome the challenge. Using a plucking-mode PEH as an example, we first established its dynamic model and converted it into an equivalent circuit. We then analyzed the energy charging–release cycle and dynamic response characteristics of the harvester. The equivalent circuit model was further used to demonstrate the superior energy transfer efficiency of the self-powered synchronous electronic charge extraction (SP-SECE) circuit. In addition, the circuit simulation incorporated an energy management module and a wireless IoT node to emulate realistic system operation. This integrated approach bridges the gap between theoretical modeling and practical application evaluation. Finally, experimental tests validated the capability of the plucking-mode PEH to enable self-powered sensing. The methods and findings presented in this work contribute a critical understanding toward improving energy harvesting efficiency and reliability, supporting the development of practical and scalable self-powered IoT systems.

Keywords: piezoelectric plucking harvester; mechanical-to-electrical energy conversion; circuit-integrated modeling; SP-SECE interface circuit.

Journal of Vibration and Acoustics. Received September 27, 2025;
Accepted manuscript posted March 2, 2026. doi:10.1115/1.4071279

1. Introduction

The rapid expansion of the Internet of Things (IoT) has greatly enhanced everyday life and industrial efficiency, yet it also introduces significant challenges in providing sustainable, maintenance-free power across varied scenarios [1-5]. This pressing need has spurred the development of efficient and reliable power supply solutions. Kinetic energy is widely present in both everyday life and industrial environments, arising from activities such as opening/closing doors/windows, vibrations from roads and bridges, and operating production lines. Harnessing widespread kinetic energy for electricity generation offers a promising route to provide continuous and efficient power for the expanding network of IoT devices. Among various energy harvesting methods, including piezoelectric [6-8], electromagnetic [9-12], and triboelectric [13-15], piezoelectric energy harvesters (PEHs) stand out for structural lightweight, easy-to-integrate, and high power density [16].

The cantilever-beam configuration with a bonded piezoelectric patch is a widely studied design for vibration energy harvesting. While effective at resonance, its operation bandwidth is narrow, and performance drops sharply once ambient vibration deviates from the tuned frequency [17]. To mitigate this limitation, a range of techniques have been developed, such as introducing nonlinearities [18, 19], using adaptive mechanisms [20, 21], or utilizing frequency up-conversion (FUC) approaches [22, 23]. Among them, magnetic or mechanical plucking has proven effective for capturing energy from ultra-low-frequency excitations [24, 25]. For example, Chen *et al*. [26] achieved higher voltage outputs with a tapered plucking beam design, while Lo *et al*. [27] improved broadband response through dual-point rotary plucking. More recent innovations integrate nonlinear sinks or hybrid mechanisms to expand harvesting duration and efficiency [28-30].

The cross-disciplinary nature of energy harvesting research is exemplified by the fact that an energy harvester is an electromechanically coupled system whose performance depends not only on mechanical design and material selection but also on the modulation of the interface circuit. In its simplest form, a conventional PEH circuit employs a bridge rectifier followed by a parallel storage capacitor [31]. Although this circuit offers simplicity and low cost, it suffers from the energy backflow issue and strong load dependence [32].

Journal of Vibration and Acoustics. Received September 27, 2025;
Accepted manuscript posted March 2, 2026. doi:10.1115/1.4071279

To address these limitations, synchronous switching harvesting on inductor (SSHI) circuits were proposed, in which a synchronized switching action is applied at the displacement extrema to invert the piezoelectric voltage [33]. This action effectively aligns the electrical voltage in phase with the mechanical velocity, ensuring that the power transferred to the electrical domain is always positive. Nevertheless, SSHI circuits still require impedance matching since the piezoelectric element remains directly connected to the load. The later-developed synchronous electric charge extraction (SECE) circuits [34] can mitigate this constraint by decoupling the energy transfer process from the energy charging phase, dividing them into two distinct stages [35]. However, conventional SECE circuits typically rely on accurate peak detection to generate switching control signals, which increases both power consumption and system complexity. To overcome this drawback, the self-powered SECE (SP-SECE) circuit was proposed [36]. It can achieve self-powered and self-sensing operation using only an envelope detector, a comparator, and an electronic breaker, thereby eliminating the need for auxiliary instruments while preserving the key advantage of the SECE technique.

To bridge the analyses of energy harvester dynamics and complex nonlinear behavior of interface circuits, equivalent circuit models (ECMs) were proposed [37-39]. While these interface circuits can enhance the power output of energy harvesters, they are insufficient to meet the practical power demands of real electronic devices. From an application standpoint, energy management modules are essential for delivering a stable voltage supply to electronic devices under varying excitation conditions. However, most previous studies on piezoelectric energy harvesting have primarily focused on interface circuit analysis, with very limited attention given to system-level simulations that incorporate both energy management modules and the power dynamics of electronic devices. This is mainly due to the absence of effective methods for establishing a truly integrated system-level model that accounts for all these factors, thereby hindering holistic investigation and enhancement of piezoelectric harvesters to meet application-level requirements.

In response to this challenge, the present work develops a system-oriented equivalent circuit representation that integrates excitation sources, harvester dynamics, interface and

Journal of Vibration and Acoustics. Received September 27, 2025;
Accepted manuscript posted March 2, 2026. doi:10.1115/1.4071279
Copyright © 2026 by ASME

management circuits, together with electronic devices, providing a unified platform for analysis and optimization. This comprehensive model allows the evaluation of the system, facilitating its holistic optimization towards practical applications. This paper is structured as follows: Section 2 details the development of the dynamic model for the plucking-mode PEH and its corresponding circuit representation. Section 3 investigates the mechanisms of energy accumulation and release during the excitation. Section 4 analyzes the power dynamics of the entire system, followed by experimental validation in Section 5. Section 6 concludes the work by highlighting the main outcomes and suggesting avenues for future investigation.

2. System Overview and Electromechanical Modelling

2.1. Mechanical structural configuration

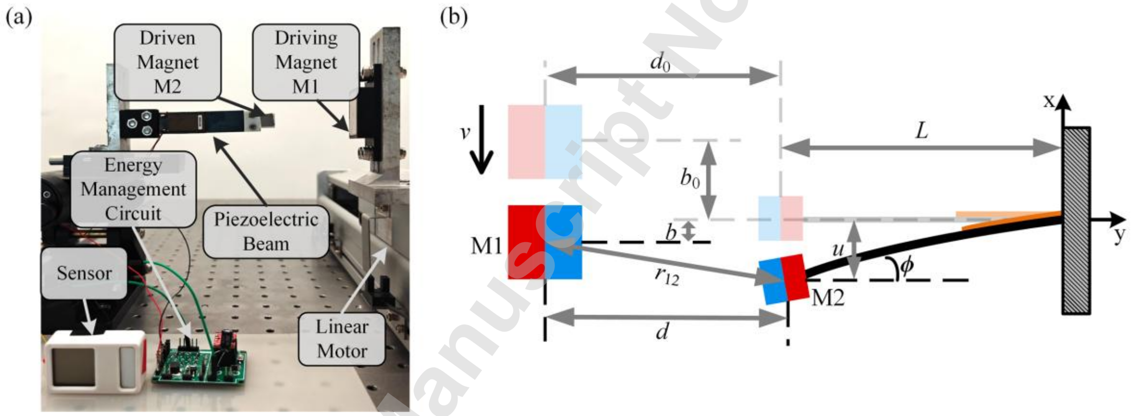

***Figure 1**. (a) Experiment setup of the PM-PEH. (b) The schematic diagram of the mechanical configuration.*

Figure 1(a) shows the fabricated prototype of the plucking-mode piezoelectric energy harvester (PM-PEH). In this design, a repulsive force is generated between a driving magnet (M1) mounted on a linear motor (Kollmorgen©, SMD175) and a driven magnet (M2) attached to the free end of a piezoelectric cantilever beam. As the linear motor moves at a constant velocity, M1 approaches the PEH, and the resulting magnetic force bends the beam and then releases it, thereby exciting underdamped vibrations. During this process, the bonded macro-fiber composite (MFC) patch transforms the beam's mechanical energy into an AC electrical output. To ensure stable operation of the downstream electronics, the

Journal of Vibration and Acoustics. Received September 27, 2025;
Accepted manuscript posted March 2, 2026. doi:10.1115/1.4071279

harvested energy is first conditioned by the SP-SECE circuit, which improves the energy conversion efficiency and delivers a reliable supply for sensor powering. **Figure 1**(b) shows the schematic representation of the mechanical configuration. In the experiments, two key parameters can be conveniently adjusted: the velocity (*v*) of the driving magnet M1 and the longitudinal spacing (*d*) between M1 and M2, which are controllable by changing the linear motor speed and its relative position, respectively. This configuration serves as the basis for the ECM developed in this work.

2.2. Dynamic model and equivalent circuit representation

During the plucking process, an external force acts on magnet M2, which is attached to the piezoelectric beam. As magnet M1 moves, it performs positive work on the beam, causing it to bend and transforming kinetic energy into elastic potential energy stored within it.

The kinetic energy supplied by the external excitation is first transformed into potential energy, consisting of the elastic energy U_e and the magnetic potential energy U_m. During the ensuing underdamped vibration, this potential energy is subsequently converted into electrical energy by the MFC. These energy components are expressed mathematically as follows:

$$U_e = \frac{1}{2} K u^2 \tag{1}$$

where u denotes the transverse displacement of the beam tip, and K is the corresponding equivalent stiffness. Using the dipole–dipole formulation [40], the interaction of M1 and M2 gives rise to the magnetic potential energy, expressed as:

$$\overrightarrow{U_m} = \overrightarrow{B_{O_2O_1}} \cdot \overrightarrow{m_1} \tag{2}$$

The magnet field $\overrightarrow{B_{O_2O_1}}$ generated by M1 at the location of M2 is given by

Journal of Vibration and Acoustics. Received September 27, 2025;
Accepted manuscript posted March 2, 2026. doi:10.1115/1.4071279

$$\vec{B}_{O_2O_1} = -\frac{\mu_0}{4\pi}\vec{\nabla}\frac{\overrightarrow{m_2}\cdot\overrightarrow{r_{12_1}}}{r_{12}^3} \tag{3}$$

where μ_0 represents the vacuum permeability and $\overrightarrow{r_{12}}$ denotes the distance vector from M1 to M2, while $\overrightarrow{m_1}$ and $\overrightarrow{m_2}$ describe the dipole moments of the two magnets. Expressions for these moment vectors are given by:

$$\overrightarrow{m_1} = \begin{bmatrix} \frac{B_r}{\mu_0}V_1 \\ 0 \\ 0 \end{bmatrix} \tag{4}$$

$$\overrightarrow{m_2} = \begin{bmatrix} \frac{B_r}{\mu_0}V_2 \\ 0 \\ 0 \end{bmatrix} \tag{5}$$

in which B_r is the residual flux density of the magnets, while B_r/μ_0 gives the magnitude of the magnetization [41]. The terms V_1 and V_2 represent the respective volumes of M1 and M2. The magnetic energy can then be expressed in scalar form as follows:

$$U_m = -\frac{\mu_0 m_1 m_2}{4\pi}\left(r_{12}^{-3} - 3d^2 r_{12}^{-5}\right) \tag{6}$$

In the above equation:

- m_1 and m_2 denote the squared magnitudes of the dipole moments $\overrightarrow{m_1}$ and $\overrightarrow{m_2}$,
- $\overrightarrow{r_{12}}$ corresponds to the squared magnitude of the separation vector r_{12},
- d specifies the longitudinal spacing between the centers of magnets M1 and M2.

ϕ designates the beam tip's angular deflection. Based on the geometry, expressions for ϕ, d, and r_{12} are derived as follows.

Journal of Vibration and Acoustics. Received September 27, 2025;
Accepted manuscript posted March 2, 2026. doi:10.1115/1.4071279

$$\phi \approx \sin^{-1}\left(u/L\right) \tag{7}$$

$$d = d_0 + L\left(1-\cos\phi\right) \tag{8}$$

$$r_{12} = \sqrt{\left(u-b\right)^2 + d^2} \tag{9}$$

where L corresponds to the distance from the beam's fixed support to magnet M2, and d_0 designates the original longitudinal distance between the two magnets. b quantifies the lateral offset between their centers. The magnet force F_m exerted by M1 on M2 can be derived from magnetic potential energy as follows [42]:

$$F_m\left(u,b\right) = \frac{-3\mu_0 m_1 m_2}{4\pi r_{12}^5}\left\{\left(u-b\right) + \frac{3du}{\sqrt{L^2-u^2}} - \frac{5d^2}{r_{12}^2}\left[\left(u-b\right) + \frac{du}{\sqrt{L^2-u^2}}\right]\right\} \tag{10}$$

To facilitate the analysis, the PM-PEH is approximated by a simplified single-DOF lumped model [43], and its governing relations can be formulated as:

$$\begin{cases} M\ddot{u} + D\dot{u} + Ku + \theta V_p + F_m\left(u,b\right) = 0 \\ \theta\dot{u} - C_p\dot{V}_p - V_p / R_p = 0 \end{cases} \tag{11}$$

where M characterizes the equivalent mass, D the damping coefficient, and V_p the electrical potential across the MFC patch. C_p, θ, and R_p correspond to the clamped capacitance of the MFC patch, its equivalent electromechanical coupling coefficient, and the external load, respectively.

After establishing the lumped-mass model, it can be readily integrated with different interface circuits for unified analysis. Specifically, in this work, we develop a system-level ECM to simulate the complete process, from external excitation to energy conversion, to energy storage, and to sensor operation. Within this framework, the motion of the magnet driving magnet M1 is emulated by a current source in parallel with a capacitor, while the magnetic interaction force is represented by a behavioral voltage source, which is defined

Journal of Vibration and Acoustics. Received September 27, 2025;
Accepted manuscript posted March 2, 2026. doi:10.1115/1.4071279

by the expression of F_m through a custom control function. According to the mechanical-electrical analogy, the parameters L_m, C_m, and R_m correspond to the effective mass, stiffness, and damping coefficient of the mechanical system, respectively. While, the MFC patch is modeled as a capacitor in parallel with a pair of arbitrary behavioral voltage and current sources, which reflect its capacitive behavior and capture the electromechanical coupling defined by the second formula in Eq. (11). This approach enables detailed analysis and optimization of the PM-PEH system, providing accurate predictions of power output and consumption under different conditions and interface circuits [44].

2.3. ***Lumped parameter identification***

An impedance-based parameter identification method is adopted to characterize the PM-PEH system's electromechanical parameters. This method enables the extraction of key equivalent circuit parameters through analysis of the system's admittance spectrum. Based on the electromechanical analogy, the equivalent circuit without magnetic force can be simplified as follows:

$$\begin{cases} R_s = R_m / \theta^2 \\ C_s = C_m \theta^2 \\ L_s = L_m / \theta^2 \end{cases} \tag{12}$$

The simplified parameters can be obtained by measuring the admittance spectrum of the PM-PEH using an impedance analyzer. **Figure 2**(a) shows the obtained admittance spectrum. The corresponding values of L_s, R_s, C_s, and C_p can be calculated based on the measured data as follows [45, 46]:

$$\begin{cases} R_s = 1 / G_{\max} \\ L_s = R_s / \left(\omega_2 - \omega_1\right) \\ C_s = \left(\omega_2 - \omega_1\right) / R_m \omega_2 \omega_1 \\ C_p = B_{\omega_s} / \omega_s \end{cases} \tag{13}$$

Journal of Vibration and Acoustics. Received September 27, 2025;
Accepted manuscript posted March 2, 2026. doi:10.1115/1.4071279

where G and B represent conductance and susceptance, respectively; ω_s denotes the resonant frequency under the short-circuit condition, B_{ω_s} is the susceptance at ω_s, and the conductance attains $1/(2G_{max})$ at ω_1 and ω_2. The electromechanical coupling coefficient θ can be determined based on the voltage response under a certain excitation [47].

As shown in **Figure 2**(b), the simulated responses are compared with the experimental measurements, and the strong agreement observed confirms the reliability of the parameter identification procedure as well as the validity of the circuit-based model. These results demonstrate that the developed framework can effectively reproduce both the dynamic characteristics and the electrical output of the energy harvester. The extracted parameters are summarized in **Table 1**.

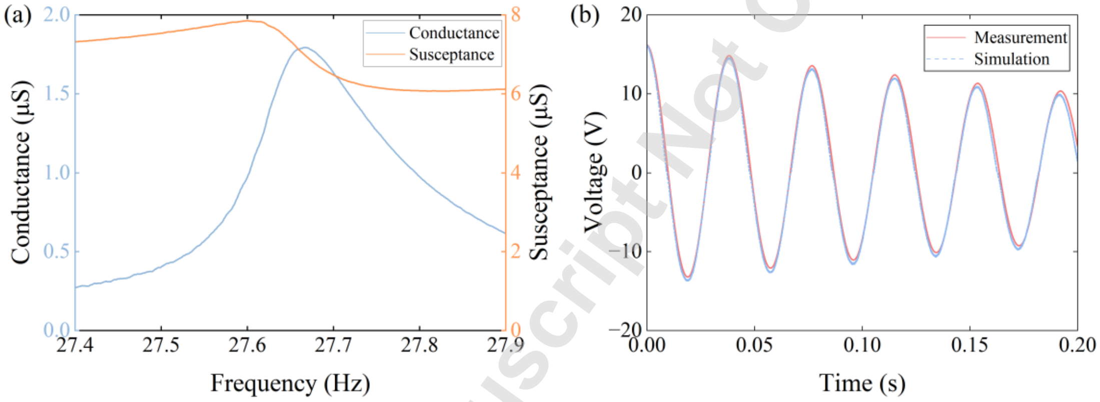

***Figure 2**. Parameter estimation and validation of the PM-PEH: (a) Admittance spectrum obtained from impedance analysis, and (b) Comparison between simulated and measured voltage responses under free-decay conditions.*

***Table 1**. Extracted physical and electrical parameters of the PM-PEH.*

Parameter	Value	Unit
M	20.12	g
D	0.14	Ns/m
K	605.92	N/m
C_p	40.22	nF
θ	0.0006664	N/m
L	86.5	mm
V_1	1000	mm^3

Journal of Vibration and Acoustics. Received September 27, 2025;
Accepted manuscript posted March 2, 2026. doi:10.1115/1.4071279

V_2	6000	mm^3
B_r	1.33	T
μ_0	$4\pi \times 10^{-7}$	H/m

3. Potential Energy Release Mechanism in the Plucking Process

This section systematically applies the theoretical model and the equivalent circuit model to analyze the behavior of the piezoelectric energy harvester during a single plucking process. The analysis is divided into two parts: quasi-static potential energy analysis and dynamic analysis. The quasi-static analysis evaluates the potential energy distribution to reveal transitions between different stability states, whereas the dynamic analysis examines the system's transient responses, including displacement and voltage outputs.

3.1. ***Quasi-static analysis***

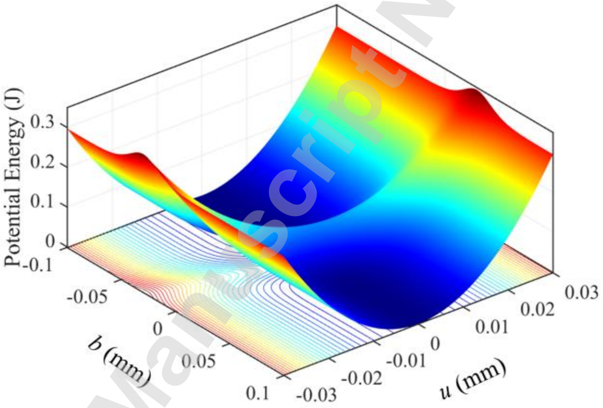

Figure 3*. Profile of total potential energy.*

In the plucking motion of the piezoelectric energy harvester, the quasi-static process refers to the phase in which the driving magnet M1 slowly approaches the driven magnet M2. During this stage, the total potential energy of the system, comprising magnetic and elastic components, undergoes significant redistribution. This process is illustrated clearly by the potential energy profiles in **Figures 3** and **4**.

Figure 3 depicts the three-dimensional distribution of the total potential energy, highlighting the ridge and trough for clearer understanding. **Figure 4** further illustrates the

Journal of Vibration and Acoustics. Received September 27, 2025;
Accepted manuscript posted March 2, 2026. doi:10.1115/1.4071279

evolution of the potential energy distribution during the movement of the driving magnet M1. Specifically, **Figure 4**(a) presents a contour map of the potential energy as a function of the driving magnet displacement b and the beam tip displacement u, providing an overview of how the potential energy landscape transforms with varying b.

Figure 4(b) to (f) illustrate specific stages of this transformation. At the initial position (b=−0.05 mm), the system has a single stable potential energy well (Well I), corresponding to a monostable state. As b increases to -0.003 mm, a secondary potential well (Well II) forms, and the system transforms into a bistable configuration. When b=0 mm, Well I and Well II are symmetrically positioned. With further increase in b, Well I gradually vanishes, leaving a monostable state dominated by Well II at b=0.003 mm. Finally, at b=0.025 mm, Well I disappears completely, and the system returns to a monostable state centred on Well II. The transition highlights the strong influence of magnet displacement (b) on the stability of the potential energy. It further suggests that the system may undergo a snap-through when a well loses stability, in which case the resulting potential-energy drop determines the timing and strength of the subsequent plucking-induced vibration.

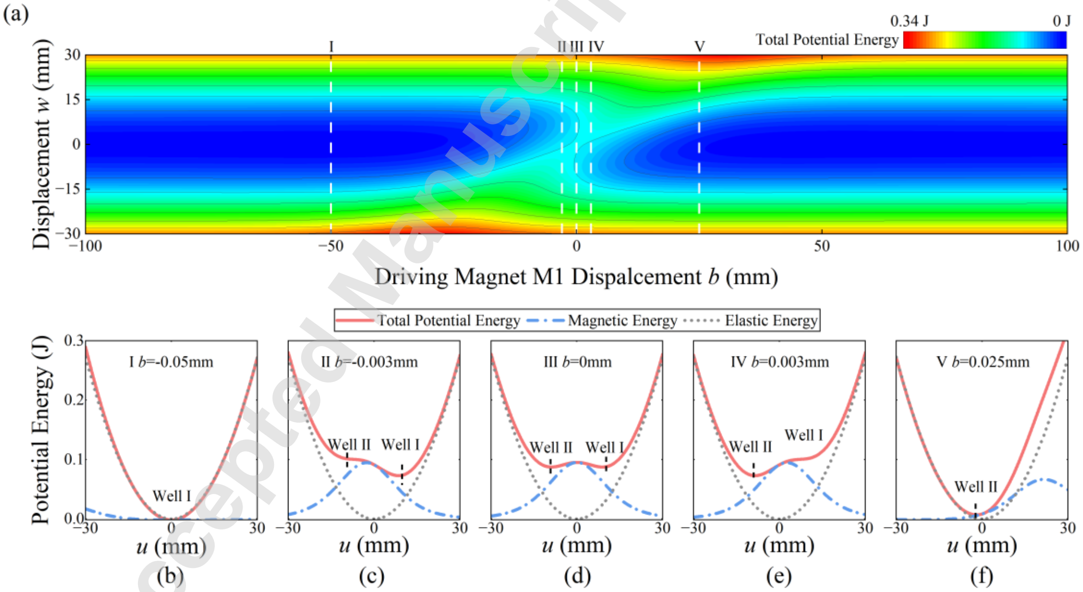

Figure 4*. The potential energy analysis. (a) Contours of total potential energy. (b)-(f) The variation of potential energy along the displacement of driving magnet M1 b: (b) Starting position with a monostable well I. (c) Critical position at which the well II appears. (d) Intermediate position with two symmetric wells. (e) Critical position at which the well I disappears. (f) Final position with a monostable well II.*

3.2. ***Dynamic analysis***

This section analyses the dynamic response of the PM-PEH under the open circuit condition during the single plucking process using the proposed ECM. Four stages are discussed, as indicated in **Figure 5**. During the simulation, d_0 is 30 mm, and the driving magnet M1 moves at a velocity of 0.4 m/s.

First, during the first stage I, the driving magnet M1 is far from the driven magnet M2. Since the interaction magnetic force between them is weak, the piezoelectric beam sits close to the equilibrium position with minor deformation, as indicated in **Figure 5**(a). Its output voltage is nearly zero in **Figure 5**(b). If M1 moves closer to M2, an increased magnetic force will deflect the piezoelectric beam during stage II. The maximum displacement of the beam is obtained at this stage because M2 rapidly deviates from the equilibrium position, while the driving magnet M1 continues to advance. As shown in **Figure 5**(a), with the gradual increase of displacement, the response voltage also rises, as illustrated in **Figure 5**(b).

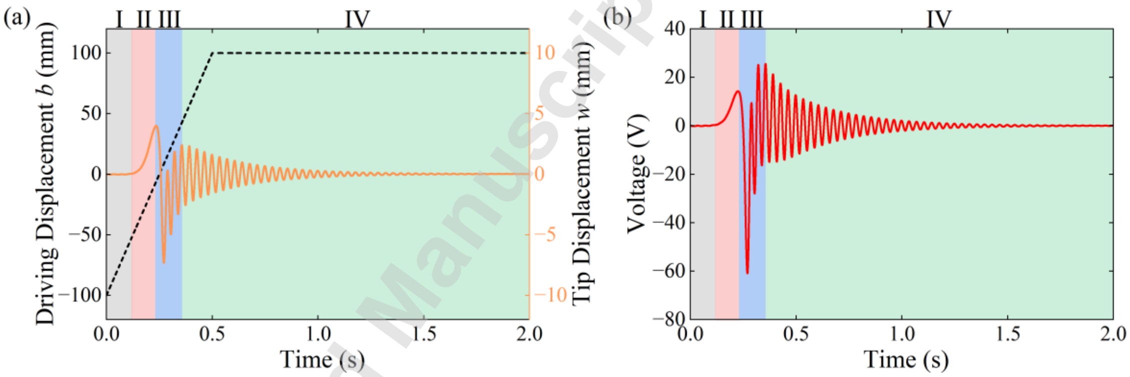

***Figure 5**. The dynamic process analysis in the time domain. (a) The displacement response of driving magnet M1 and driven magnet M2. (b) The voltage response.*

Once magnet M1 moves beyond the critical position, the repelling force can no longer offset the elastic deformation of the beam. As a result, the beam is released and enters an oscillatory state. In stage III, the beam displacement becomes asymmetric, as shown in **Figure 5**(a), since M1 remains within the effective vibration range. This asymmetry is also evident in the voltage waveform in **Figure 5**(b), where the voltage peaks on one side are higher than on the other. In the final stage IV, as the driving magnet M1 moves farther

Journal of Vibration and Acoustics. Received September 27, 2025;
Accepted manuscript posted March 2, 2026. doi:10.1115/1.4071279

from M2, the magnetic force becomes negligible. The beam thus vibrates symmetrically around its equilibrium position. As shown in **Figure 5**, both the displacement and voltage waveforms return to symmetry.

Furthermore, the equivalent circuit model is employed to evaluate the influences of different initial distances d_0. **Figure 6**(a) illustrates the time-voltage response of the system under varying initial distances ($d_0 = 30$, 25, and 20 mm). As d_0 decreases, the peak voltage increases, indicating that more energy is captured during the plucking process due to the stronger magnetic interaction between M1 and M2. This phenomenon is further analyzed using the phase portraits shown in **Figures 6**(b)-(d), where a smaller d_0 leads to a larger limit position b_c, implying a higher input-energy requirement to trigger the plucking event. Physically, reducing d_0 enhances the magnetic force gradient, resulting in a larger vibration amplitude and higher electrical output. However, this improvement comes at the cost of higher input energy, since a stronger interaction also raises the energy barrier that must be overcome to initiate plucking. Therefore, selecting a proper initial distance is essential to balance energy capture efficiency with input demand.

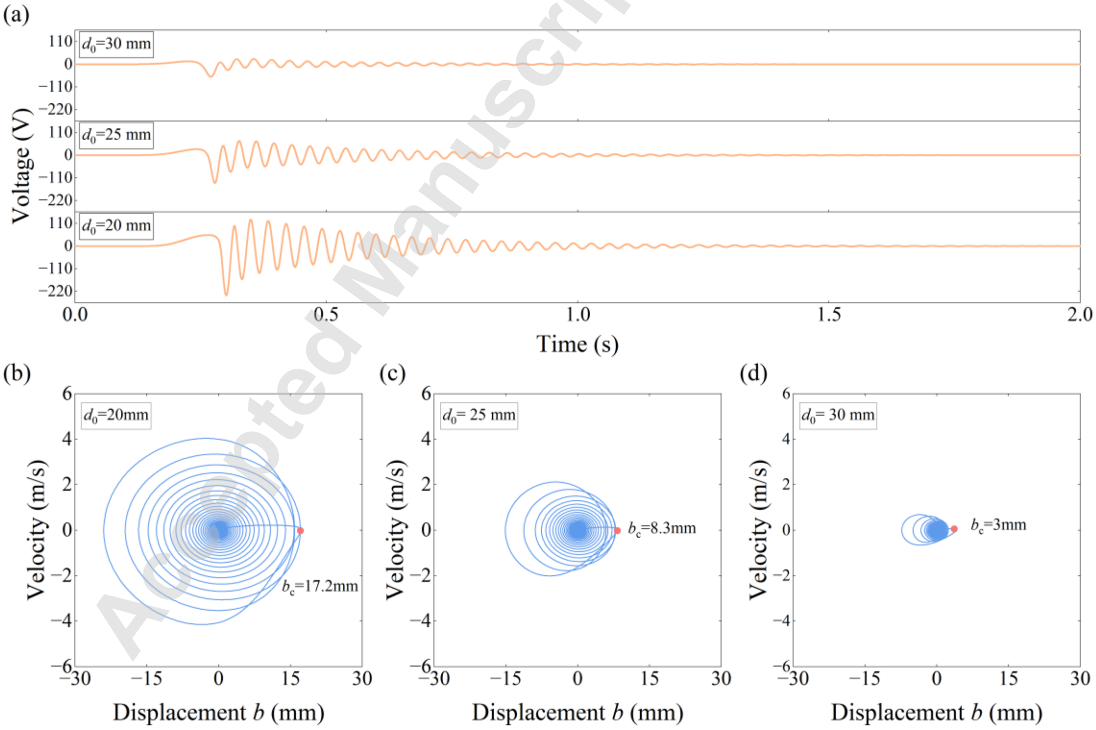

Figure 6. *Simulation result of time-voltage response and phase portrait under different d_0. (a) The voltage waveform. (b)-(d) phase portrait: (b) d_0=20 mm, (c) d_0=25 mm, (d) d_0=30 mm.*

Journal of Vibration and Acoustics. Received September 27, 2025;
Accepted manuscript posted March 2, 2026. doi:10.1115/1.4071279

4. Analysis of Interface Circuit and Energy Management Module

While the analyses of potential energy distribution and dynamic responses clarify the fundamental mechanisms governing the output performance, achieving reliable power delivery in real-world applications requires further optimization. In particular, the design of advanced interface circuits and the integration of efficient energy management modules are critical for minimizing energy losses, stabilizing output, and ensuring adaptability across diverse scenarios.

To provide a comprehensive assessment of the PM-PEH system, we developed an equivalent circuit model that captures the entire energy harvesting process—from magnetic plucking excitation to piezoelectric conversion, interface circuit operation, and final energy delivery through the power management module, as illustrated in **Figure 7**. System-level simulations were conducted in LTspice, and subsequent experimental validation confirmed the accuracy and robustness of the proposed model.

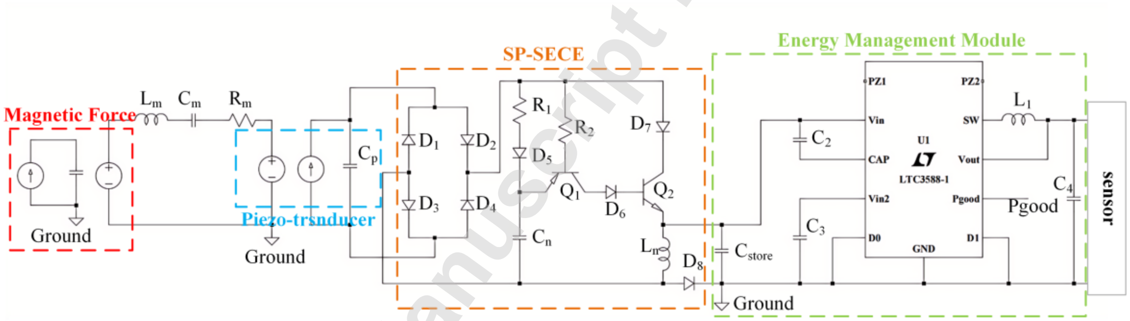

Figure 7. *Comprehensive schematic illustrating the system-level equivalent circuit framework.*

4.1. ***SP-SECE interface circuit analysis***

The SP-SECE is an effective nonlinear interface that employs synchronized switching to improve energy-harvesting performance. By overcoming key limitations of conventional interface designs—such as energy backflow issue and strong load independence—the SP-SECE circuit can significantly enhance the energy harvesting efficiency, particularly for weakly and moderately coupled electromechanical systems.

Journal of Vibration and Acoustics. Received September 27, 2025;
Accepted manuscript posted March 2, 2026. doi:10.1115/1.4071279

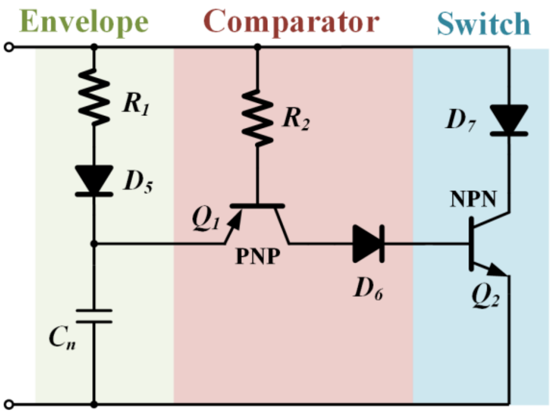

***Figure 8**. The three primary functional components of the electronic breaker.*

Conventional implementations of the SECE circuit rely on external equipment. To realize self-powered and self-sensing operation, additional circuitry for peak detection and switch control is usually required. In this work, we adopt a self-powered SECE (SP-SECE) configuration that employs an electronic breaker to achieve a truly self-powered interface. As shown in **Figure 8**, the SP-SECE architecture incorporates an envelope detector, a comparator, and a switch. The operating principle of the electronic breaker is described as follows. As the mechanical oscillator moves from the equilibrium position toward the displacement peak, the piezoelectric capacitor C_p is charged, and the piezoelectric voltage V_p rises toward its maximum value V_{pM}. In parallel, the envelope capacitor C_n is also charged. Owing to the existence of R_1 and D_5, the peak of V_{cn} occurs slightly later than that of V_p and is slightly lower than V_{pM}. Afterward, this peak value of V_{cn} is preserved on C_n, while V_p begins to decrease as the oscillator reverses its motion direction. During this interval, the magnitude of the base–emitter voltage of the PNP transistor Q_1 increases until it exceeds the turn-on threshold, at which point Q_1 starts to conduct. Consequently, C_n discharges through Q_1 and D_6, which then drives Q_2 into conduction. The conduction of Q_2 switches on the LC oscillation loop, enabling C_p to be rapidly discharged to approximately zero. The residual energy in C_n is then balanced through the emitter–collector path of Q_1 with that in C_p, ensuring that C_n maintains the same voltage polarity as C_p before the reverse cycle begins. As a result, the envelope detector can operate properly over the entire vibration cycle.

Journal of Vibration and Acoustics. Received September 27, 2025;
Accepted manuscript posted March 2, 2026. doi:10.1115/1.4071279

Table 2. *Component list of the SP-SECE circuit.*

Designator	Part number	Variable	Value
$D_{1\text{-}8}$	NSR02100HT1G	L_n	1 mH
Q_1 (PNP)	MMBT5401	C_n	3 nF
Q_2 (NPN)	MMBT5551	C_{store}	47 µF

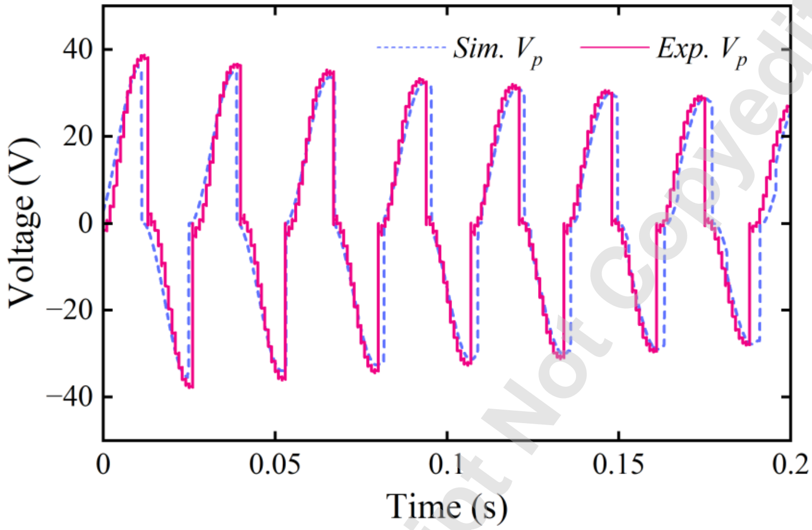

Figure 9*. Comparison of simulated and experimental voltage waveforms across the clamped capacitance of the piezoelectric transducer integrated with the SP-SECE circuit.*

More importantly, the active components used for peak detection and switch control, typically implemented using a complementary pair of PNP and NPN transistors, can be readily modelled and simulated in standard circuit simulation software. This facilitates the systematic analysis and design optimization. Therefore, the SP-SECE circuit is well-suited to the proposed self-powered system and is adopted as the primary interface circuit in this study.

The electronic components used in the SP-SECE circuit are outlined in **Table 2**. Using the identified system parameters of both PM-PEH and SP-SECE, **Figure 9** compares the simulated and experimental voltage waveforms under open-circuit conditions. The close match validates the parameter identification procedure and demonstrates the accuracy of the proposed equivalent circuit model in capturing system dynamics.

Journal of Vibration and Acoustics. Received September 27, 2025;
Accepted manuscript posted March 2, 2026. doi:10.1115/1.4071279
Copyright © 2026 by ASME

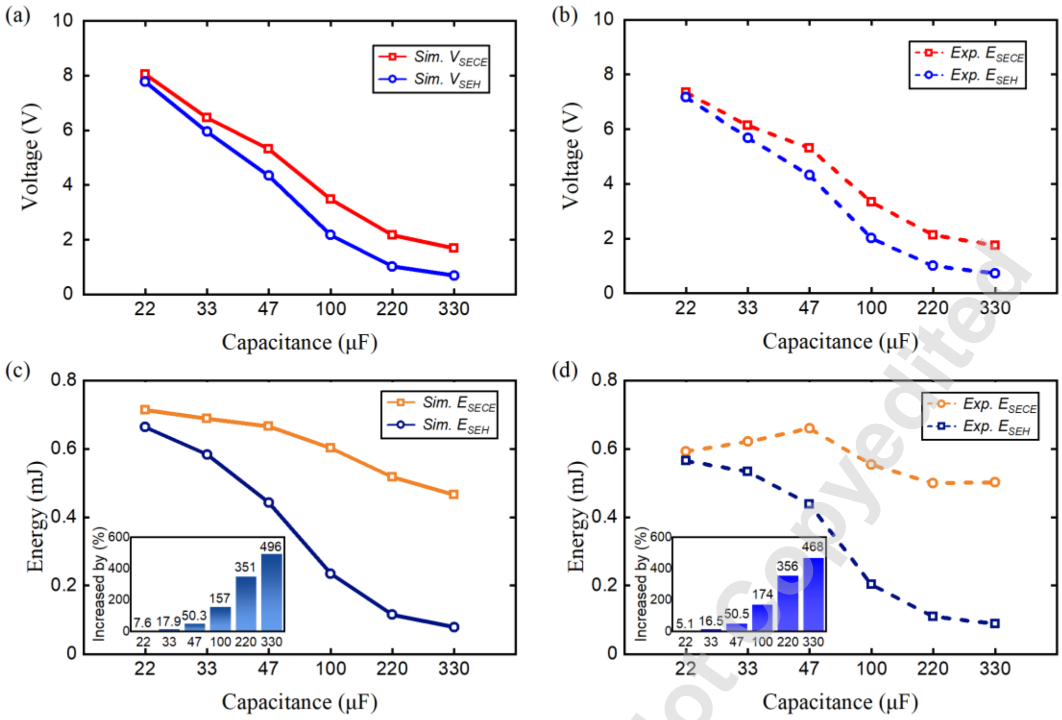

***Figure 10**. Charging performance comparison of SEH and SP-SECE circuits under varying storage capacitances. (a) Simulated and (b) experimental charging voltage; (c) simulated and (d) experimental stored energy.*

The charging performance of the SP-SECE circuit was evaluated via both simulation and experiment, and the results are shown in **Figure 10**. For comparison, a conventional PEH circuit, consisting of a bridge rectifier and a parallel storage capacitor [31], which is commonly referred to as the standard energy harvesting (SEH) circuit, was also tested. The charging voltage and stored energy of the SP-SECE and SEH circuits were analyzed across capacitances of 22, 33, 47, 100, 220, and 330 μF. In these cases, the initial longitudinal separation d_0 was set to 26 mm, and the initial transverse distance b_0 was set to -0.1 m.

As shown in **Figure 10**(a) and (c), the simulation results reveal that the SP-SECE circuit achieves higher efficiency than the SEH circuit, with its superiority becoming more pronounced at larger capacitance values. The experimental results presented in **Figure 10**(b) and (d) show the same trend that the SP-SECE circuit delivers consistently higher charging voltage and stored energy across all tested capacitances. Specifically, with a 22 μF storage capacitor, the SP-SECE circuit achieves 8.06 V and 714.60 μJ, compared with 7.77 V and

Journal of Vibration and Acoustics. Received September 27, 2025;
Accepted manuscript posted March 2, 2026. doi:10.1115/1.4071279

664.10 μJ for the SEH circuit. For the storage capacitor with 330 μF, the values become 1.74 V, 501.85 μJ, and 0.73 V, 88.01 μJ, respectively.

The improved charging performance is attributed to the operating mechanism of the SP-SECE circuit, which decouples energy transfer and energy charging into two separate stages. By performing synchronous charge extraction, the SP-SECE circuit can effectively mitigate the energy backflow issue that commonly occurs in the conventional SEH circuit. Moreover, the increasingly pronounced superiority of the SP-SECE circuit at larger storage capacitances indicates its load-independent behavior. In contrast, under the same excitation, increasing the storage capacitance changes the effective electrical impedance of the SEH circuit, leading to a greater deviation from the maximum power transfer condition and, consequently, a more significant efficiency degradation.

Overall, the simulation and experimental results exhibit good agreement, verifying the effectiveness of the equivalent circuit model. Although a minor discrepancy is observed, the consistent trend further highlights the superior effectiveness of the SP-SECE circuit in improving energy extraction under varying storage conditions.

4.2. ***Energy management module simulation***

Previous studies have primarily employed equivalent circuit models to investigate interface circuits and analyze energy extraction mechanisms. This work extends equivalent circuit modeling to simulate power management modules and sensor operation. By incorporating the energy management module and an equivalent sensor load into the circuit representation, the proposed model enables comprehensive system-level analysis that bridges energy harvesting, storage, and utilization.

To validate this capability, we implemented the energy management module using the LTC-3588 chip and tested it with both SP-SECE and SEH circuits powering a temperature and humidity sensor. The LTC3588 is a high-efficiency low-power management IC that integrates a programmable undervoltage lockout (UVLO) function, which allows the self-powered system to accumulate energy in the storage capacitor until a predefined turn-on threshold is reached. In this experiment, the motor moved at a constant velocity of 0.4 m/s. The initial longitudinal separation and transverse distance were set to d_0=28 mm and b_0 = -0.1 m, respectively. The output voltage of the LTC3588-1 module was set to 1.8 V

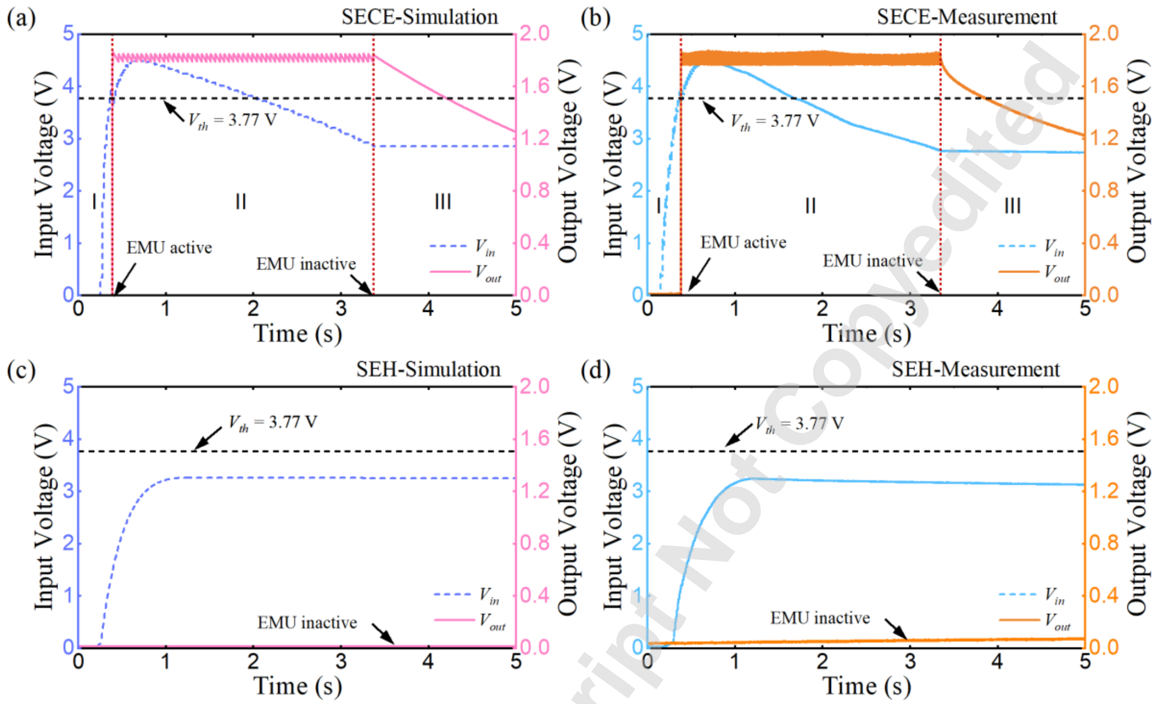

***Figure 11**. Simulated and experimental responses of the SP-SECE and SEH circuits when connected to the energy management module supplying the temperature and humidity sensor. Panels (a, b) show SP-SECE behavior, and panels (c, d) display the SEH counterpart.*

Figure 11 compares the simulated and experimental results, where the equivalent sensor load is represented by a constant resistor in LTspice to replace the physical device. The close agreement between simulation and experiment confirms the reliability of the model in capturing the behavior of the energy management module and sensor operation. This validation demonstrates the model's ability to predict critical operating states, such as voltage thresholds and activation behavior. The simulation results further reveal the superior performance of the SP-SECE circuit in enhancing energy harvesting efficiency. As shown in **Figure 11**(a) and (b), the SP-SECE circuit enables the storage capacitor voltage to exceed the activation threshold, thereby successfully powering the sensor. In contrast, the SEH circuit fails to reach this threshold in both the simulation and experiment, preventing activation of the energy management module.

Journal of Vibration and Acoustics. Received September 27, 2025;
Accepted manuscript posted March 2, 2026. doi:10.1115/1.4071279

A detailed investigation of sensor operation reveals three successive stages. Phase I – Startup: At this stage, the SP-SECE interface charges the storage capacitor, and the input voltage gradually rises until it surpasses the activation limit of the EMU, 3.77 V. This progression is clearly reflected in both the simulated and measured waveforms. Phase II – Sensor Operation: Once triggered, the management module delivers a steady 1.8 V supply to drive the temperature and humidity sensor, maintaining operation for about three seconds, as illustrated in **Figures 11**(a) and (b). Phase III – Power Outage: When the stored charge in the capacitor is exhausted, the input voltage drops below the activation point, which disables the power management unit and causes the sensor to shut down.

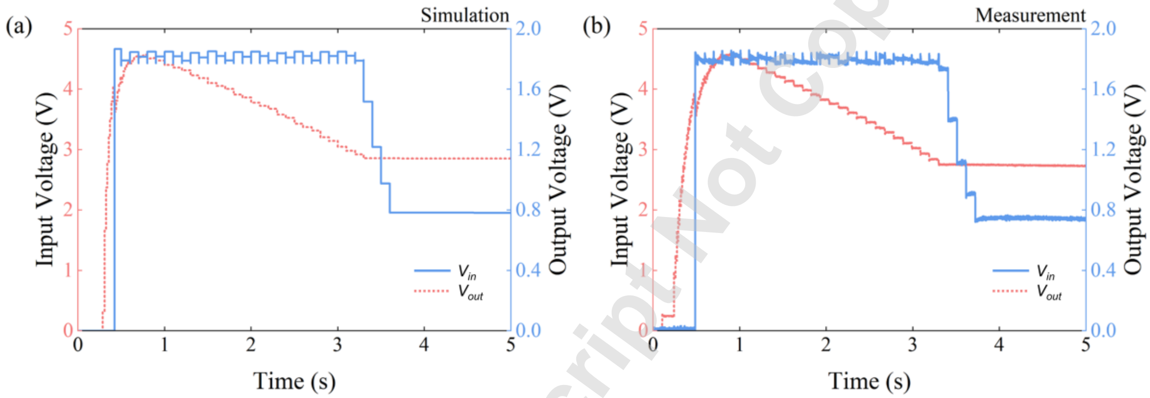

***Figure 12**. Comparison between simulation and experimental results for a wireless signal transmitter with SP-SECE circuit: (a) Simulation result of input and output voltage of the energy management module. (b) Experimental results of the input and output voltage of the energy management module.*

Further validation of the proposed system-level ECM was extended to a wireless IoT sensing node. Unlike the temperature and humidity sensor, which operates continuously once activated, the wireless IoT node sends intermittent signals every 0.1 seconds. In this case, a time-varying resistor is adopted to emulate the dynamic power demand of the IoT node. **Figure 12** shows a comparison of the wireless IoT node's simulated response with experimental data. The model effectively captures the activation threshold behavior of the energy management module and the periodic power dynamic patterns of the transmitter during operation. Minor discrepancies between the simulated and experimental results are observed during the shutdown stage, primarily due to changes in the sensor's internal load characteristics after it ceases operation. This deviation reflects the dynamic nature of real-world load behavior, which the equivalent circuit model can approximate but not fully

Journal of Vibration and Acoustics. Received September 27, 2025;
Accepted manuscript posted March 2, 2026. doi:10.1115/1.4071279

replicate. Future refinements could incorporate dynamic load modeling to enhance simulation accuracy. The results demonstrate that, once the energy management module is activated, it delivers a stable output voltage to the wireless IoT node, enabling signal transmission every 0.1 seconds. This validates the model's capability to predict transient energy demands and the dynamic behavior of intermittent-load devices.

This section has validated the developed system-level ECM by showcasing its ability to accurately simulate the energy management module and sensor operation. Under identical excitation conditions, the SP-SECE circuit enabled the harvester to exceed the activation threshold voltage and ensure stable sensor operation, whereas the SEH circuit did not. The demonstrated capability to operate with both continuous and intermittent load devices emphasizes its adaptability for practical use.

5. Experimental Validation of the Holistic Power Dynamics

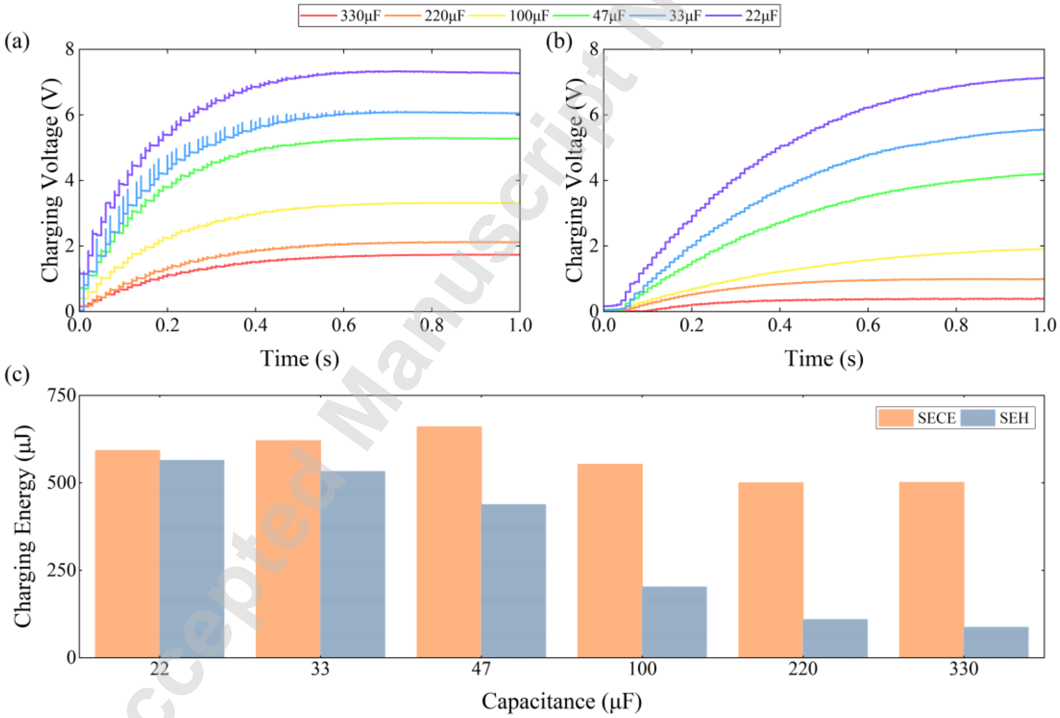

***Figure 13**. Charging performance comparison. Charging voltage curves in SP-SECE circuit (a) and SHE circuit (b). (c) Charging energy.*

This section presents an experimental investigation of the output performance of the PM-PEH system, where b_0 and d_0 were primarily set to -0.1 m and 26 mm. As shown in

Journal of Vibration and Acoustics. Received September 27, 2025;
Accepted manuscript posted March 2, 2026. doi:10.1115/1.4071279

Figure 13, the SP-SECE circuit exhibits superior charging performance compared with the SEH circuit. The capacitor charging curves in **Figures 13**(a) and (b) demonstrate that the SP-SECE circuit achieves both a higher charging rate and a higher charging voltage. A comparison of charging energy in **Figure 13**(c) further highlights the advantage of SP-SECE over SEH. **Figure 14** analyzes the effect of different plucking velocities, showing that in the test of charging a 47 μF capacitor, the SP-SECE circuit consistently outperforms the SEH circuit across all tested velocities. Moreover, the results indicate that the SP-SECE circuit maintains stable performance regardless of the velocity of the driving magnet, underscoring its suitability for practical scenarios with unpredictable motion conditions.

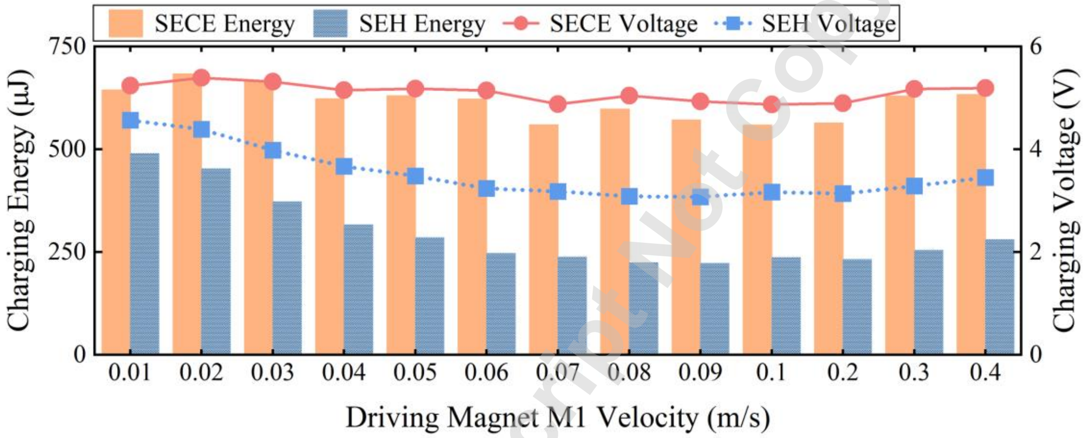

***Figure 14**. Charging voltage and energy comparison of the SP-SECE and SEH circuit with different moving velocities.*

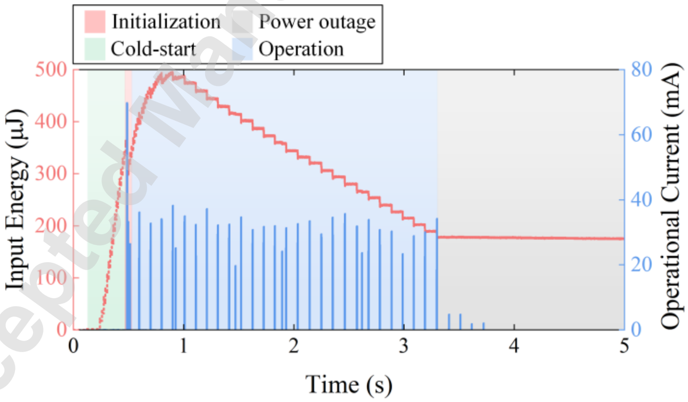

***Figure 15**. Workflow of the wireless IoT node.*

Figure 15 illustrates the workflow of the PM-PEH powering a wireless IoT node, further evaluating its practicality in real applications. Once sufficient energy is harvested, the system operates through four stages defined by the input energy level and the device's

Journal of Vibration and Acoustics. Received September 27, 2025;
Accepted manuscript posted March 2, 2026. doi:10.1115/1.4071279

operating current. Immediately after the cold-start phase, the storage capacitor charges to the activation threshold of the energy management module. Once powered, the system drives the transmitter to broadcast signals every 0.1 seconds. When the stored energy is depleted, the system enters the power-outage phase, during which the device ceases operation.

Further experimental investigations in this section confirm the robustness and stability of the PM-PEH system under variable motion conditions, demonstrating its capability to power wireless devices and its practicality for energy-constrained applications.

6. Conclusion

This paper has presented a comprehensive analysis of a plucking-mode piezoelectric energy harvester (PM-PEH) to address significant gaps in modeling, analyzing, and optimizing the energy harvesting process. To this end, the dynamic model was developed and transformed into the equivalent circuit model, obtaining a systematic understanding of the PM-PEH's electromechanical coupling behavior. Further, an impedance measurement-based identification procedure ensured the developed equivalent circuit model's accuracy and reliability. The quasi-static potential energy conversion and the dynamic response were analyzed to explain the basic mechanism responsible for energy harvesting. System-level equivalent circuit simulations revealed the benefits of employing a self-sustained SP-SECE interface, which enhances energy transfer efficiency. Building on this, the circuit modeling framework was further expanded to incorporate the power management stage and sensor operation, enabling an integrated system-level simulation that effectively links theoretical analysis with practical application. The experimental verification confirmed the superiority of the proposed PM-PEH system, which could reliably power sensors and wireless IoT devices. This work offers a comprehensive circuit simulation approach along the complete energy conversion chain. The findings provide a solid foundation for further research and practical deployment of self-powered systems, especially in IoT applications and other energy-constrained situations.

Journal of Vibration and Acoustics. Received September 27, 2025;
Accepted manuscript posted March 2, 2026. doi:10.1115/1.4071279

Acknowledgement

This study was financially supported by the National Natural Science Foundation of China (Grant No. 52305135), Guangzhou Municipal Science and Technology Project (Grant No. 2023A03J0011), and Guangdong Provincial Project (Grant No. 2023QN10L545).

References

[1] Li, Z., X. Peng, G. Hu, D. Zhang, Z. Xu, Y. Peng, and S. Xie, *Towards real-time self-powered sensing with ample redundant charges by a piezostack-based frequency-converted generator from human motions.* Energy Conversion and Management, 2022. **258**.

[2] Li, Y., Y. Wang, Y. Li, X. Peng, D. Li, X. Xia, X. Li, Y. Zi, and G. Hu, *Heat-powered IoT node: A synergistic fusion of thermoacoustic engine and triboelectric nanogenerator.* Applied Physics Letters, 2025. **126**(2).

[3] Wang, Y., H. Du, H. Yang, Z. Xi, C. Zhao, Z. Qian, X. Chuai, X. Peng, H. Yu, and Y. Zhang, *A rolling-mode triboelectric nanogenerator with multi-tunnel grating electrodes and opposite-charge-enhancement for wave energy harvesting.* Nature Communications, 2024. **15**(1): p. 6834.

[4] Li, Y., Y. Li, Y. Wang, M. Xiao, H. Tang, Y. Zi, J. Wang, X. Li, W.-H. Liao, and G. Hu, *From nature's deadly strike to safety protection: Mantis shrimp-inspired ultrafast energy transformation for smart surveillance.* Device, 2025.

[5] Du, C., S. Jiang, S. Qu, X. Wang, Y. Zhang, C. Lan, and G. Hu, *Vehicle-Level Modeling and Analysis of Onboard Energy Harvesters and Their Impact on Dynamics.* Journal of Vibration and Acoustics, 2025. **147**(6): p. 061009.

[6] Sezer, N. and M. Koç, *A comprehensive review on the state-of-the-art of piezoelectric energy harvesting.* Nano Energy, 2021. **80**.

[7] Zhang, L., J. Kan, S. Lin, W. Liao, J. Yang, P. Liu, S. Wang, and Z. Zhang, *Design and performance evaluation of a pendulous piezoelectric rotational energy harvester through magnetic plucking of a fan-shaped hanging composite plate.* Renewable Energy, 2024. **222**.

[8] S, S., Y. V, V. S, S.K. S, and M. H, *Design of Piezoelectric-Enabled Wireless Sensor Nodes: Self-Powered Solutions*, in *2023 Intelligent Computing and Control for Engineering and Business Systems (ICCEBS)*. 2023. p. 1-7.

[9] Carneiro, P., M.P. Soares dos Santos, A. Rodrigues, J.A.F. Ferreira, J.A.O. Simões, A.T. Marques, and A.L. Kholkin, *Electromagnetic energy harvesting using magnetic levitation architectures: A review.* Applied Energy, 2020. **260**.

[10] Miao, G., S. Fang, S. Wang, and S. Zhou, *A low-frequency rotational electromagnetic energy harvester using a magnetic plucking mechanism.* Applied Energy, 2022. **305**.

[11] Sarker, M.R., M.H.M. Saad, J.L. Olazagoitia, and J. Vinolas, *Review of Power Converter Impact of Electromagnetic Energy Harvesting Circuits and Devices for Autonomous Sensor Applications.* Electronics, 2021. **10**(9).

[12] Li, Y., X. Peng, Y. Li, D. Li, and G. Hu, *Catapult mechanism-enabled push-button energy harvester designed for capturing ultra-low frequency motion.* Mechanical Systems and Signal Processing, 2025. **225**: p. 112268.

Journal of Vibration and Acoustics. Received September 27, 2025;
Accepted manuscript posted March 2, 2026. doi:10.1115/1.4071279

[13] Xin, C., Z. Li, Q. Zhang, Y. Peng, H. Guo, and S. Xie, *Investigating the output performance of triboelectric nanogenerators with single/double-sided interlayer.* Nano Energy, 2022. **100**.

[14] Xin, C., Z. Xu, X. Xie, H. Guo, Y. Peng, Z. Li, L. Liu, and S. Xie, *Structure-Crack Detection and Digital Twin Demonstration Based on Triboelectric Nanogenerator for Intelligent Maintenance.* Adv Sci (Weinh), 2023. **10**(26): p. e2302443.

[15] Kang, X., P. Li, Y. Wang, R. Zhang, Y. Li, Y. Jian, Q. Su, G. Hu, and J. Wang, *A Nonlinear Galloping-Driven Triboelectric-Electromagnetic Hybrid Generator for Low-Speed Wind Energy Harvesting.* Green Energy and Intelligent Transportation, 2025: p. 100363.

[16] Fu, H. and E.M. Yeatman, *Effective piezoelectric energy harvesting using beam plucking and a synchronized switch harvesting circuit.* Smart Materials and Structures, 2018. **27**(8).

[17] Rosso, M., A. Nastro, M. Bau, M. Ferrari, V. Ferrari, A. Corigliano, and R. Ardito, *Piezoelectric Energy Harvesting from Low-Frequency Vibrations Based on Magnetic Plucking and Indirect Impacts.* Sensors (Basel), 2022. **22**(15).

[18] Caetano, V.J. and M.A. Savi, *Star-shaped piezoelectric mechanical energy harvesters for multidirectional sources.* International Journal of Mechanical Sciences, 2022. **215**.

[19] He, L., L. Liu, J. Zhou, G. Yu, B. Sun, and G. Cheng, *Design and analysis of a double-acting nonlinear wideband piezoelectric energy harvester under plucking and collision.* Energy, 2022. **239**.

[20] Tian, W., Z. Zhao, W. Liu, Q. Zhu, Z. Zhang, and Y. Yuan, *Analysis on the power and bandwidth improvement of a frequency-tuning optimized SECE circuit.* Sensors and Actuators A: Physical, 2021. **332**.

[21] Hu, G., J. Liang, C. Lan, and L. Tang, *A twist piezoelectric beam for multi-directional energy harvesting.* Smart Materials and Structures, 2020. **29**(11).

[22] Wu, Y., S. Li, K. Fan, H. Ji, and J. Qiu, *Investigation of an ultra-low frequency piezoelectric energy harvester with high frequency up-conversion factor caused by internal resonance mechanism.* Mechanical Systems and Signal Processing, 2022. **162**.

[23] Li, Z., X. Peng, G. Hu, and Y. Peng, *Theoretical, numerical, and experimental studies of a frequency up-conversion piezoelectric energy harvester.* International Journal of Mechanical Sciences, 2022. **223**.

[24] Ahmad, M.M., N.M. Khan, and F.U. Khan, *Review of frequency up‐conversion vibration energy harvesters using impact and plucking mechanism.* International Journal of Energy Research, 2021. **45**(11): p. 15609-15645.

[25] Noh, J., S. Bae, Y.J. Yoon, and P. Kim, *Nonlinear Dynamic Analysis of a Piezoelectric Energy Harvester with Mechanical Plucking Mechanism.* Sensors (Basel), 2023. **23**(13).

[26] Chen, K., S. Fang, Z. Lai, J. Cao, and W.-H. Liao, *A plucking rotational energy harvester with tapered thickness and auxetic structures for increasing power output.* Applied Energy, 2024. **357**.

[27] Lo, Y.C., C.C. Chen, Y.C. Shu, and M.F. Lumentut, *Broadband piezoelectric energy harvesting induced by mixed resonant modes under magnetic plucking.* Smart Materials and Structures, 2021. **30**(10).

[28] Shen, J., S. Wan, J. Fu, S. Li, D. Lv, and K. Dekemele, *A magnetic plucking frequency up-conversion piezoelectric energy harvester with nonlinear energy sink structure.* Applied Energy, 2024. **376**.

[29] Shen, J., S. Wan, J. Fu, S. Li, D. Lv, and K. Dekemele, *A magnetic plucking frequency up-conversion piezoelectric energy harvester with nonlinear energy sink structure.* Applied Energy, 2024. **376**: p. 124326.

[30] Bahmanziari, S. and A.-A. Zamani, *A new framework of piezoelectric smart tiles based on magnetic plucking, mechanical impact, and mechanical vibration force mechanisms for electrical energy harvesting.* Energy Conversion and Management, 2024. **299**: p. 117902.

Journal of Vibration and Acoustics. Received September 27, 2025;
Accepted manuscript posted March 2, 2026. doi:10.1115/1.4071279

[31] Ottman, G.K., H.F. Hofmann, A.C. Bhatt, and G.A. Lesieutre, *Adaptive piezoelectric energy harvesting circuit for wireless remote power supply.* IEEE Transactions on power electronics, 2002. **17**(5): p. 669-676.

[32] Liang, J. and W.-H. Liao, *Energy flow in piezoelectric energy harvesting systems.* Smart materials and structures, 2010. **20**(1): p. 015005.

[33] Guyomar, D., A. Badel, E. Lefeuvre, and C. Richard, *Toward energy harvesting using active materials and conversion improvement by nonlinear processing.* IEEE transactions on ultrasonics, ferroelectrics, and frequency control, 2005. **52**(4): p. 584-595.

[34] Lefeuvre, E., A. Badel, C. Richard, and D. Guyomar, *Piezoelectric energy harvesting device optimization by synchronous electric charge extraction.* Journal of intelligent material systems and structures, 2005. **16**(10): p. 865-876.

[35] Tang, H., W. Liu, G. Hu, J. Liu, and D. Dong, *Optimized multi-step synchronous electric charge extraction via accurate electrical efficiency analysis.* Smart Materials and Structures, 2025. **34**(2): p. 025027.

[36] Zhu, L., R. Chen, and X. Liu, *Theoretical analyses of the electronic breaker switching method for nonlinear energy harvesting interfaces.* Journal of Intelligent Material Systems and Structures, 2012. **23**(4): p. 441-451.

[37] Zhang, Z., H. Xiang, and L. Tang, *Modeling, analysis and comparison of four charging interface circuits for piezoelectric energy harvesting.* Mechanical Systems and Signal Processing, 2021. **152**.

[38] Liu, Z., G. Hu, X. Li, C. Zhao, and Y. Yang, *Equivalent circuit modeling for triboelectric energy harvesters.* Mechanical Systems and Signal Processing, 2025. **235**: p. 112916.

[39] Tang, H., X. Peng, X. Li, D. Yu, Y. Zi, and G. Hu, *A unified system-level simulation framework for energy harvesting, management, and application in plucking piezoelectric energy harvesters.* Smart Materials and Structures, 2025. **34**(5): p. 05LT01.

[40] Griffiths, D.J., *Introduction to electrodynamics.* 2023: Cambridge University Press.

[41] Coey, J.M., *Permanent magnet applications.* Journal of Magnetism and Magnetic Materials, 2002. **248**(3): p. 441-456.

[42] Yung, K.W., P.B. Landecker, and D.D. Villani, *An analytic solution for the force between two magnetic dipoles.* Physical Separation in Science and Engineering, 1998. **9**(1): p. 39-52.

[43] Stanton, S.C., C.C. McGehee, and B.P. Mann, *Nonlinear dynamics for broadband energy harvesting: Investigation of a bistable piezoelectric inertial generator.* Physica D: Nonlinear Phenomena, 2010. **239**(10): p. 640-653.

[44] Wang, J., L. Luo, D. Yurchenko, and G. Hu, *Equivalent Circuit Analysis of a Nonlinear Vortex-Induced Vibration Piezoelectric Energy Harvester Using Synchronized Switch Technique.* IEEE Transactions on Industrial Electronics, 2024: p. 1-12.

[45] Hoseyni, S.M., A. Aghakhani, and I. Basdogan, *Experimental admittance-based system identification for equivalent circuit modeling of piezoelectric energy harvesters on a plate.* Mechanical Systems and Signal Processing, 2024. **208**.

[46] Kuang, Y., Z.J. Chew, and M. Zhu, *Strongly coupled piezoelectric energy harvesters: Finite element modelling and experimental validation.* Energy Conversion and Management, 2020. **213**.

[47] Lefeuvre, E., A. Badel, A. Brenes, S. Seok, M. Woytasik, and C.S. Yoo, *Analysis of piezoelectric energy harvesting system with tunable SECE interface.* Smart Materials and Structures, 2017. **26**(3).